Chapter 3
Current State of the Art of Modelling and Simulation of Propulsion Systems for Hybrid Electric Aircraft

Isil Yazar, Ranjan Vepa and Fikret Caliskan

Nomenclature

Abstract

The environmental problems caused by fossil fuels have bolstered the need for research and development of "clean" propulsion systems to power future transport. Both academia and industry are focusing their research on alternative fuels and sustainable resources for developing effective, efficient, and clean future vehicle propulsion systems to reduce their effect on the environment. The aviation industry is closely following the development in electrical vehicle technology in the automotive sector, but many challenges remain, such as those related to certification. Many prototypes for electric aircraft have already been built and tested. However, restrictions due to technological limitations, as well as development costs, have imposed significant constraints on proposed designs. One way to reduce these initial costs is via mathematical models that can simulate the entire system before any real hardware is built, so that designs and parameters can be optimised cost-effectively. This review paper describes the state-of-the-art on hybrid propulsion component modelling for two key components: a high-temperature superconducting permanent magnet synchronous motor and a lithium-air battery. It is based on an examination of current published literature. These components could be essential in delivering a clean and efficient energy source for propelling an electric aircraft in the future. The work also gives information about literature studies of fault detection in batteries.

I.Yazar[1] (✉), R.Vepa[2], F. Caliskan[3]
[1]Eskisehir Osmangazi University, Eskisehir, Turkiye
[2]Queen Mary University of London, London, United Kingdom
[3]Istanbul Technical University, Istanbul, Turkiye
e-mail: iyazar@ogu.edu.tr

Keywords: Hybrid Electric Propulsion Systems, Mathematical Modelling, Battery, HTS Motors and Generators, Fault Detection in Batteries.

3.1. Introduction

Nowadays, aviation is faced with the risk of increasing fuel prices, limited fuel resources and negative contribution of fuel usage on the environment. This has resulted in a new hot topic entitled "sustainable aviation" for both aviation academia and the aviation industry. By means of this new terminology, electric propulsion technology takes the place of conventional internal combustion engine (ICE) powered propulsion partially or completely. Studies on this subject revealed three main different topologies for propulsion systems. In electric propulsion systems, conventional ICE is completely removed from the system and electric motors that are powered by energy storage components become main propulsive. Turbo electric propulsion system combines conventional ICE and electric motors with a suitable power grid and provides ICE powered electric propulsive force. Hybrid electric propulsion system is an energy storage component embedded version of turbo electric propulsion system. Energy storage components can be classified as batteries, fuel cells, super capacitors and so on. Hybridization is provided by partial usage of both ICE and energy storage components.

According to literature, there are many ongoing studies about hybrid and turbo electric propulsion systems. Tay et al (Tay et al, 2018) developed a model as a software tool for comprehensive flight performance and mission analysis of hybrid-electric aircraft. A simulation software named as PLA.N.E.S. (PLAtform for New Environment-friendly Solutions) has developed and validated for the assessment of performance, costs and environmental impact of conventional and advanced configuration aircraft topics by Donateo et al (Donateo et al, 2016). Design and performance evaluation of a hybrid electric power system oriented to multicopters is proposed by Donatea et al (Donateo et al, 2017). Sziroczak et al (Sziroczak et al, 2020), Pornet and Isikveren (Pornet and Isikveren, 2015) evaluated conceptual design studies related to hybrid electric powered aircrafts. A novel sizing and optimization approach for series-hybrid unmanned convertiplane is studied by Chen et al (Chen et al, 2020). Riboldi (Riboldi, 2019) proposed energy-optimal power management for hybrid-electric aircraft using off-design characteristics. Brelje and Martins (Brelje and Martins, 2019) presented a detailed literature review work for novel propulsion system structures considering fundamentals, products, prototypes, concepts and so on. Baumeister et al (Baumeister et al, 2020) examines the emission reduction potentials of First Generation Electric Aircraft (FGEA) in Finland. Xie et al (Xie et al, 2020) reviewed current technological developments of hybrid electric propulsion system powered aircraft and also its conceptual design and energy management methodologies. A preliminary weight sizing technique proposed for General Aviation electric aircraft is evaluated in (Riboldi et al, 2018a). Another sizing study is studied by Vratny and Hornung (Vratny and Hornung, 2018) on electric power train components and options of the electric motor powering a ducted fan for hybrid electric aircraft. Gong et al (Gong et al,2016) simulated the performance of a fuel-cell powered hybrid propulsion system for a small unmanned aircraft. Ji et al (Ji et al, 2020) searched

performance characteristics of a solid oxide fuel cell powered hybrid jet engine for various operating modes. Xie et al (Xie et al, 2019) presented a fuzzy logic based equivalent energy consumption optimization study for hybrid electric powered UAV. Donateo and Spedicato (Donateo and Spedicato, 2017) focused on a formulation of fuel economy/endurance for a hybrid electric aircraft. They also proposed updates on existing battery discharge models and charging models for lithium batteries with validations. They evaluated battery specifications and the engine working points on fuel economy on a parallel hybrid power system. Donateo et al (Donateo et al, 2018) achieved detailed information about the power demand of a rotorcraft along different mission profiles and they made estimation for how much energy and power should be supplied during various hybridization schemes. Ribeiro et al (Ribeiro et al, 2020) proposed a method for incorporating hybrid-electric propulsion in the conceptual design phase and made environmental analysis of various hybrid/electric aircraft. Riboldi (Riboldi, 2018b) mentioned the preliminary design difficulties of new propulsion technologies and suggested an optimal approach to cope with them. In turbine-less solid oxide fuel cell powered hybrid electric jet engines, the compressor component is directly driven by the fuel cell. Ji et al (Ji et al, 2020) determined a safe operation zone for unmanned aerial vehicle by means of this structure. Rohacs and Rohacs (Rohacs and Rohacs, 2020) drew attention to the energy factors to compare aircrafts powered by different various propulsion systems. Sliwinski et al (Sliwinski et al, 2017) proposed a Hybrid Electric Propulsion System retrofit design methodology for existing Remotely Piloted Aircraft Systems.

In this work, current mathematical model studies of hybrid electric propulsion systems from literature are evaluated. The paper is organised as follows. The methodology belongs to the novel propulsion systems is illustrated in Section 2. Section 3 presents the mathematical models of hybrid electric propulsion system components. As a conclusion, future projections are discussed in Section 4.

3.2. Methodology

Electrification applications in aviation have been started with the more-electric aircraft (MEA) concept. Airbus A380 and Boeing 787 are the well-known examples of this concept (Roboam, 2011). By means of MEA, some key updates are observed in design, construction and operation procedures of aircraft. To reduce aircraft weight problem, operating costs, power consumption and to enhance maintainability; electrical system substructure is preferred instead of hydraulic, mechanical and/or pneumatic system usage (Gnadt et al, 2019).

Novel propulsion system arrangements can be categorised in three main topics. These are hybrid-electric, turbo-electric and all electric propulsion systems respectively. Hybrid electric structures can be categorised in three subtitles: Series hybrid electric, parallel hybrid electric and series/parallel partial hybrid electric. In series hybrid electric structures, electrical propulsion is generated from electric motors that are powered by gas turbine generated electrical power and/or battery (or any energy storage component). In parallel hybrid electric structures, a battery powered motor and a turbine engine are both located on a shaft which drives a fan, thus, either

or both generate propulsive power. The series/parallel partial hybrid electric one is an arrangement of individual structures. Turbo electric is the energy storage component-less form of series hybrid electric configurations. Partial turbo electric structure is another arrangement of turbo electric propulsion (National Academies of Sciences, Engineering, and Medicine, 2016).

From the point of specific energy, energy storage components will be strongly decisive for definition of prior servicing structure/s. Comparing liquid fuels with batteries, conventional fuels still provide 50 times more specific energy than batteries and this has an important effect on endurance (Brelje and Martins, 2019). Thus, it is predicted that the progress will continue in turbo electric, hybrid electric and all electric manner due to technological developments.

3.3. Mathematical Model Studies

3.3.1. Power System Level Architecture Concepts

In conventional aircrafts, electrical systems do not have a serious contribution to the aircraft weight. Thus, weight estimations for conceptual design are made relatively easily without considering electrical architectures. With the transition from mechanical thrust to electrical thrust, electrical architectures became more important in terms of performance, weight and flight safety (Brelje and Martins, 2019). Armstrong et al, (2015) proposed various power system architectures for the N3-X aircraft using turboelectric propulsion system structure and also pointed out another study related to architecture, voltage and components for proposed architectures (Gemin et al, 2017). Considering the proposed architectures, some literature studies show that mathematical model simulations belonging to proposed power system architectures are conducted using today's conventional gas turbine data (Yazar, 2019; Sener et al, 2020a; Sener et al, 2020b).

3.3.2. Power Electronics Component Models

High Temperature Superconducting (HTS) Materials Based Electric Motors

Electric motors are generally made up of electro-magnets which in turn have a large number of copper wire windings. The length of the copper wire used in the winding makes the resistance quite significant. Thus they dissipate heat and as a result of the energy dissipation are not 100% efficient. Additional losses are also caused by mechanical friction, which can be minimised and by eddy current losses and the hysteresis. To maximise the efficiency of energy conversion the losses must be reduced to a minimum. This can be done by reducing the resistance of the wire, eliminating the eddy current losses and providing compensation to minimise the hysteresis. To achieve efficiencies as high as 99%, the resistance of the windings must be reduced substantially and practically to zero. This is indeed feasible by using high temperature superconducting materials for the winding rather than copper wire. HTS materials are superconducting materials that exhibit the superconducting property at relatively higher temperatures than normal superconducting materials.

In most metallic conductors, although the resistance decreases as the temperature is reduced, there is still a significant resistance to current flow even as the temperature reaches low values close to absolute zero. In a superconductor there exists a critical temperature below which there is a sudden drop in its resistance to a value very near to zero. The material is able to conduct an electrical current almost without any loss of energy. A superconducting loop would permit the current to flow around it indefinitely. In a normal superconductor, the critical temperature below which the resistivity drops dramatically is almost equal to absolute zero. Thus the material must be cooled using liquid helium, with a boiling point of -269°C (4°K). In high-temperature superconductors the critical temperature below which the resistivity drops dramatically is much higher and around -200°C. Thus the cooling can be achieved by using liquid nitrogen, which has a boiling point of -196°C (77°K). Thus the use of HTS wires for motor windings has the capacity to allow for the design of electric motors with very high efficiencies because the electrical resistance of the wire is practically eliminated. The higher critical temperature of the HTS wires means that the energy required by the cryostat to cool the superconducting windings is also much lower. In fact, the higher the critical temperature, the lower is the energy required by the cryostat. Several researchers have reported the existence of the property of superconductivity just below -23°C, albeit under the application of high pressures. This allows for the possibility of reducing the energy required by a cryostat to a minimum at high altitudes of flight. However, the complete lack of resistance in the windings can cause the motors to be unstable at times. But the continued presence of eddy current and hysteresis losses means that there is just enough resistance to ensure that the motor is stable at its operating speed. Figure 3.1 illustrates the typical responses of an uncontrolled HTS synchronous motor.

Fig. 3.1.   Typical responses of an uncontrolled HTS synchronous motor
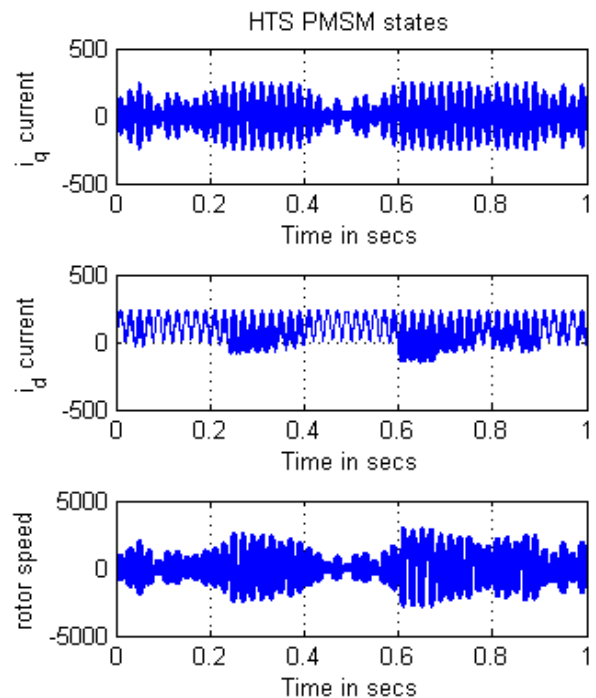
The property of high temperature superconductivity however facilitates the design of lightweight and completely controllable motors with a high thrust as well as a high power to weight capacity of the order of 20 kW/Kg. In a typical HTS AC synchronous motor the losses are reduced by more than 50% when compared with standard iron-core induction motors. Consequently, by allowing small HTS AC synchronous motors to drive either open or ducted propellers located at several points along the leading edges of the wings and tail plane, it is possible in principle to generate higher lift, thereby increasing the aerodynamic efficiency of the lifting surfaces, as well as higher levels of lift than in conventional aircraft. Moreover, HTS synchronous motors may be modelled and controlled as normal synchronous motors but with a much lower stator resistance (Vepa, 2018).

Dynamic Modelling Of HTS Synchronous Motors

The dynamic modelling of a typical three phase permanent magnet synchronous motor (PMSM) is briefly revisited. The mathematical modelling is based on a number of assumptions including, 1) The stator windings are balanced and the magneto motive force (MMF) is sinusoidal; 2) The variation of the inductance with the rotor position is sinusoidal; 3) All changes in the saturation conditions as well as changes in the parameters are ignored; 4) These type of machines is generally assumed to have balanced three-phase windings. The inputs are also balanced. The direct (*d*)- and quadrature (*q*)-coordinate frame is based on an equivalent circuit model that is commonly used for the modelling of PMSMs. The three phase equations relating the stator phase voltages $\begin{bmatrix} V_a & V_b & V_c \end{bmatrix}$ to the stator resistances R_s, stator phase currents $\begin{bmatrix} I_a & I_b & I_c \end{bmatrix}$, and the phase flux linkages $\begin{bmatrix} \lambda_a & \lambda_b & \lambda_c \end{bmatrix}$ are,

$$\begin{bmatrix} V_a \\ V_b \\ V_c \end{bmatrix} = R_s \begin{bmatrix} I_a \\ I_b \\ I_c \end{bmatrix} + \frac{d}{dt} \begin{bmatrix} \lambda_a \\ \lambda_b \\ \lambda_c \end{bmatrix}$$

(3.1)

The flux linkages are related to the inductance matric and the phase flux linkages provided by the permanent magnets by,

$$\begin{bmatrix} \lambda_a \\ \lambda_b \\ \lambda_c \end{bmatrix} = \begin{bmatrix} L_{aa} & L_{ab} & L_{ac} \\ L_{ab} & L_{bb} & L_{bc} \\ L_{ac} & L_{bc} & L_{cc} \end{bmatrix} \begin{bmatrix} \lambda_{a,pm} \\ \lambda_{b,pm} \\ \lambda_{c,pm} \end{bmatrix} = \begin{bmatrix} L_{aa} & L_{ab} & L_{ac} \\ L_{ab} & L_{bb} & L_{bc} \\ L_{ac} & L_{bc} & L_{cc} \end{bmatrix} \begin{bmatrix} \cos\theta \\ \cos(\theta - 2\pi/3) \\ \cos(\theta + 2\pi/3) \end{bmatrix} \lambda_{pm}$$

(3.2)

The input power is,

$$P_i = \begin{bmatrix} V_a & V_b & V_c \end{bmatrix} \begin{bmatrix} I_a & I_b & I_c \end{bmatrix}^T .$$

(3.3)

To convert any three phase quantity in $a-b-c$ frame to the $d-q-0$ frame, Parks transformation is used. It is defined as,

$$\begin{bmatrix} s_q \\ s_d \\ s_0 \end{bmatrix} = \frac{2}{3} \begin{bmatrix} \cos\theta & \cos(\theta-2\pi/3) & \cos(\theta+2\pi/3) \\ \sin\theta & \sin(\theta-2\pi/3) & \sin s(\theta+2\pi/3) \\ 1/2 & 1/2 & 1/2 \end{bmatrix} \begin{bmatrix} s_a \\ s_b \\ s_c \end{bmatrix} .$$

(3.4)

The inverse relation is,

$$\begin{bmatrix} s_a \\ s_b \\ s_c \end{bmatrix} = \begin{bmatrix} \cos\theta & \sin\theta & 1 \\ \cos(\theta-2\pi/3) & \sin(\theta-2\pi/3) & 1 \\ \cos(\theta+2\pi/3) & \sin s(\theta+2\pi/3) & 1 \end{bmatrix} \begin{bmatrix} s_q \\ s_d \\ s_0 \end{bmatrix} .$$

(3.5)

An alternate view of the transformation is to transform from the $a-b-c$ frame to another stator fixed frame, the $\alpha-\beta$ frame, followed a transformation to the $d-q$ axes, given by,

$$\begin{bmatrix} s_\alpha \\ s_\beta \end{bmatrix} = \frac{2}{3} \begin{bmatrix} 1 & \cos(2\pi/3) & \cos(4\pi/3) \\ 0 & \sin(2\pi/3) & \sin(4\pi/3) \end{bmatrix} \begin{bmatrix} s_a \\ s_b \\ s_c \end{bmatrix}, \quad \begin{bmatrix} s_\alpha \\ s_\beta \end{bmatrix} = \begin{bmatrix} \cos\theta & -\sin\theta \\ \sin\theta & \cos\theta \end{bmatrix} \begin{bmatrix} s_d \\ s_q \end{bmatrix}$$

(3.6)

With these transformations the voltages in the stator may be expressed in the $d-q$ axes of PMSM by the equations,

$$\begin{bmatrix} v_d \\ v_q \end{bmatrix} = R \begin{bmatrix} i_d \\ i_q \end{bmatrix} + \frac{d}{dt} \begin{bmatrix} \lambda_d \\ \lambda_q \end{bmatrix} + \omega_s \begin{bmatrix} 0 & -1 \\ 1 & 0 \end{bmatrix} \begin{bmatrix} \lambda_d \\ \lambda_q \end{bmatrix}$$

(3.7)

where $\lambda_q = L_q i_q$ and $\lambda_d = L_d i_d + \lambda_{pm}$. Hence the input power may be expressed as,

$$P_i = \begin{bmatrix} V_a & V_b & V_c \end{bmatrix} \begin{bmatrix} I_a & I_b & I_c \end{bmatrix}^T = \frac{3}{2} \begin{bmatrix} v_d & v_q \end{bmatrix} \begin{bmatrix} i_d & i_q \end{bmatrix}^T \tag{3.8}$$

Using the equations for $\begin{bmatrix} v_d & v_q \end{bmatrix}$, which may also be presented as $\mathbf{V}_{ref} = v_d + j v_q$, in steady state and ignoring the dissipation, the output power is given by,

$$P_o = \frac{3\omega_s}{2} \begin{bmatrix} \lambda_d & \lambda_q \end{bmatrix} \begin{bmatrix} 0 & 1 \\ -1 & 0 \end{bmatrix} \begin{bmatrix} i_d \\ i_q \end{bmatrix} = \frac{3\omega_s}{2} \begin{bmatrix} -\lambda_q & \lambda_d \end{bmatrix} \begin{bmatrix} i_d \\ i_q \end{bmatrix} = \frac{3\omega_s}{2} \left(\lambda_d i_q - \lambda_q i_d \right) \tag{3.9}$$

Eliminating the fluxes in the $d - q$ axes, the output power simplifies to,

$$P_o = \frac{3\omega_s}{2} \left(\lambda_d i_q - \lambda_q i_d \right) = \frac{3\omega_s}{2} \left(\lambda_{pm} i_q + \left(L_d - L_q \right) i_q i_d \right) \tag{3.10}$$

The mechanical speed ω is related to the electrical frequency by $\omega_s = P\omega/2$, where P is the number of poles. Hence the torque exerted by the stator on the rotor, which is the sum of the synchronisation and reluctance components, is obtained by dividing the output power by the mechanical speed and is,

$$T_e = \frac{3}{2} \frac{P}{2} \left(\lambda_{pm} i_q + \left(L_d - L_q \right) i_q i_d \right) \tag{3.11}$$

The total mechanical load torque, including the actual load, the inertia load and the friction loss, balances the driving torque and consequently,

$$T_e = \frac{3}{2} \frac{P}{2} \left(\lambda_{pm} i_q + \left(L_d - L_q \right) i_q i_d \right) = T_L + J \frac{d\omega}{dt} + B_f \omega \tag{3.12}$$

Direct Torque Control of HTS Synchronous Motors

One objective in designing a controller is to ensure steady state operation. This implies that in a reference frame fixed in the stator, rather than the $d - q - 0$ frame that is fixed in the rotor,

the mechanical speed of the rotor is steady. The basic principle of direct torque control is to control the electromagnetic torque and stator flux of the synchronous motor by selecting the input voltages using an appropriate modulation technique. A stator fixed reference frame is used to control both the flux and torque independently. Applying suitable coordinate transformations, the voltage, flux linkage and current can be transformed from one reference frame to another. Therefore, the torque equation in the synchronous speed reference frame can be written as,

$$\begin{bmatrix} s_x \\ s_y \end{bmatrix} = \begin{bmatrix} \cos\delta & \sin\delta \\ -\sin\delta & \cos\delta \end{bmatrix} \begin{bmatrix} s_d \\ s_q \end{bmatrix}$$
$$,$$

(3.13)

where, $\sin\delta = \lambda_q \big/ \sqrt{\lambda_q^2 + \lambda_d^2} = \lambda_q \big/ |\lambda|$, $\cos\delta = \lambda_d \big/ \sqrt{\lambda_q^2 + \lambda_d^2} = \lambda_d \big/ |\lambda|$. The normalised torque equation may be expressed as,

$$\frac{4T_e}{3P} = \lambda_d i_q - \lambda_q i_d = \lambda_d \left(i_x \sin\delta + i_y \cos\delta \right) - \lambda_q \left(i_x \cos\delta - i_y \sin\delta \right) = i_y |\lambda|$$

(3.14)

The equation (3.14) now indicates that the torque output of the motor is proportional directly to the y – component of the stator current when the amplitude of the stator flux linkage is held fixed.

To introduce the application of pulse width modulation (PWM) in switching the three phases in a sequence, the three phases will be represented as phasors and the input signal is represented as a weighted sum. A three phase voltage input is converted to a signal $\mathbf{V}_{ref} = |\mathbf{V}_{ref}| e^{j\delta}$ with a magnitude of and a phase angle δ. Such a representation can be implemented by a voltage source inverter (VSI) to convert a DC input to a controlled three phase output. A voltage phasor is represented as,

$$\mathbf{V}_{ref} \equiv \mathbf{V}_s = \frac{2}{3} V_{dc} \left(S_a + e^{j2\pi/3} S_b + e^{j4\pi/3} S_c \right) = \frac{2}{3} V_{dc} \left(S_a + \mathbf{a} S_b + \mathbf{a}^2 S_c \right)$$

(3.15)

Integrating the stator phase voltage equation, phase flux linkages may be expressed, with and without the resistive losses, respectively as,

$$\lambda_s - \lambda_s |_{t=0} = \mathbf{V}_s t - \int_0^t R_s \mathbf{i}_s dt \qquad \lambda_s - \lambda_s |_{t=0} = \mathbf{V}_s t$$
$$,$$

(3.16)

Thus it may be observed that the time variation of the stator flux linkage phasor is in the same form as the given voltage vector and therefore, it is possible to control the amplitude and vector components by proper selection of the voltage input phasor.

Fig. 3.2. Generating the input sequence.
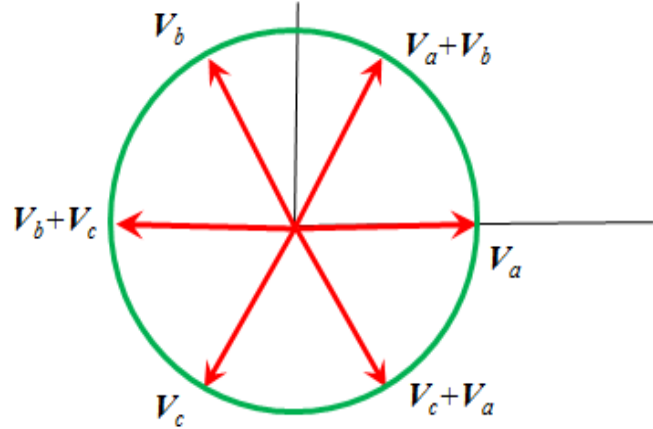
The three phases are separated by a phase angle difference of $\delta = 2\pi/3$. By adding the first two phases, a vector that leads the first phase by $\pi/3$ is created. By adding the next two phases, a vector that is the negative of the first phase is created. Finally by adding the third and the first phase, a vector that lags the first phase by $\pi/3$ is created. This can be diagrammatically represented as in Figure 3.2. By sequencing the input phases to follow the input as in Figure 3.2, one can ensure that the output torque is also a rotating vector of constant magnitude. This is the principle of direct torque control and the details are outlined in (Ozcira and Bekiroglu, 2018). Direct torque control is implemented by selecting a proper voltage space vector according to a switching sequence which is coded as a table and used as a reference input voltage selector for the VSI. Thus the reference vector rotates anticlockwise as the motor rotates through one revolution. The input signal depends upon the error values between the measured and reference values of the linkage flux and the output torque. The reference values are obtained by sensing the motor phase voltage and phase currents followed by voltage and current calculations in the stationary reference frame. The reference voltage vector is calculated by using the active voltage vector on which sample lies and the zero vectors for different times over a sample time frame.

Using equation (16), the change in the rotor flux over the sampling period ΔT is,

$$\Delta \lambda_s = \mathbf{V}_s \Delta T$$

(3.17)

Then, by applying a proportional integral control law, one could estimate the desired change in the flux and calculate a new reference voltage phasor which is then available for conversion to a three-phase output by the VSI.

Once this is done all that remains is to obtain the sampling times over the sector of each vector and the switching sequence, which would then determine the three-phase input to the synchronous motor, completing the input control loop. Direct torque control of a synchronous machine is completely feasible (and desirable) even in the absence of any resistive losses as in a HTS motor.

3.3.4 Batteries and Fault Detection in Batteries

Lithium-metal and Lithium-Air are currently considered as the best material for designing light-weight batteries with high power output densities. Lithium has the highest energy density and consequently batteries could run twice as long. Lithium air batteries can hold more energy than the universally used lithium-ion batteries.

Lead acid batteries and nickel metal hydride (NiMH) batteries have been used in electric vehicles (EV) for many decades and are considered to be mature technologies for battery development. Lithium ion (Li-ion) cells are now used as standard for assembling modern battery packs for electric vehicles. There are many types of Li-ion batteries, assembled from Li-ion cells, that each have widely varying characteristics, but vehicle manufactures generally require excellent longevity. Li-ion battery packs have many benefits when compared with other mature battery packs. By using both the current, voltage and temperature measurements, battery packs can be modelled so that the parameters associated with their internal dynamics can be estimated. This in turn allows one to develop fast algorithms to predict the state of health and state of charge for secure and long endurance operations.

Full Order Modelling of The Lithium Air Cell

The electro-chemical modelling and simulation of an electrolyte generally requires the precise representation of the dynamics of the movement of multiple species of mobile ions and other constituents. These elements and constituents must obey transport laws that are applicable to binary and/or dilute / concentrated solutions. These transport laws are usually based on the conservation of mass, momentum and Nernst-Planck equations. The internal generation of various species due to the specific input processes, are governed by the conservation of mass or continuity equation for the concentration of the species, in terms of the flux of the species and the number of moles of the species per unit volume per second generated during the processes. The flux density gives the number of moles travelling per unit time across a plane of unit area that is perpendicular to the flow of species. The flux is a result of the movement of the species due to the local existence of an electric field, and/or the diffusion of the species due to the presence of a gradient in the concentration, and/or the influence of convection. Neglecting the convective term, the equation for flux generation or the equation describing the transportation of the species can

be expressed as the sum of two terms due to the motion of the species in an electric field and due to a concentration gradient in terms of the mobility, the electrostatic potential, the concentration and the diffusion coefficient, all associated with a particular species within the electrolyte.

Charge transport within an electrolyte for dilute solutions is governed by equations that are applicable to Li-air batteries with dual electrolytes prior to the saturation of the electrolytes. The theory of dilute solutions can be applied to Li-air batteries with an aqueous electrolyte, when the concentration of electrolyte is well below saturation. Concurrently, the theory of concentrated solutions can be applied to Li-air batteries with dual electrolytes or an organic electrolyte beyond the saturation limit. The Stefan-Maxwell multi-component diffusion equation describes the interaction between the diffusive fluxes of two species in a concentrated solution or a gas mixture. It is the basis of the concentrated solution theory which relates the electrochemical potential applied to a species to its average velocity and its diffusion coefficient. The multi-component diffusion equation for the concentrated solutions is expressed in terms of the friction coefficients and the relative average velocities of the species.

The output voltage of a Li-air battery can be expressed in terms of concentrations of Li ions and of oxygen, the electrostatic potentials of the Li ions and of the electrons and the porosity of the carbon electrode. To construct a discrete domain model, the concentration dynamics of Li ions and that of oxygen are modelled by one-dimensional diffusion dynamics. The electro-static potentials are defined by two steady state one-dimensional Poisson equations, while the concentrations are defined by unsteady diffusion equations. The porosity is a reducing variable defined by a first order rate equation. The complete model is reduced initially to a set of finite state equations and eventually to a set of discrete state equations.

Ion Transport in The Electrolyte

The modelling and simulation of the transportation of ions with an electrolyte solution generally requires an accurate description of the movement of species of multiple mobile ions and other non-ionic constituents. Transport laws that are appropriate for the solutions of binary and/or dilute / concentrated concentrations are adopted to perform the simulations. The species transportation laws are commonly based on the continuity equation or the conservation of mass and the Nernst-Planck equations. Following Bevara (Bevara, 2015), the species conservation equation with the presence of the internal generation of a species i due to the inputs, is:

$$\frac{\partial C_i}{\partial t} = -\nabla \cdot \mathbf{N}_i + G_i$$

(3.18)

where the concentration of the species in mol/cm³ is C_i, $\mathbf{N}_i$ is the molar flux of the species in mol/cm²s, and G_i represents the number of moles of the species per cubic cm per second formed due to other processes.

The molar flux density $\mathbf{N}_i$ gives the molar flux rate travelling across a plane of unit area that is perpendicular to the flow of species i. This is the molar flux that is in existence due to the result of the motion of the species under the influence of the local electric field, and/or diffusion of the species under the influence of a gradient in the concentration, and/or the result of convection. Neglecting the convection effects, the general equation for molar flux or the equation describing the species motion can be written as the sum of two terms due to movement of the species in an electric field and due to the action of the concentration gradient, as,

$$\mathbf{N} = -u_i C_i \nabla \phi_i - D_i \nabla C_i$$

(3.19)

where u_i is the mobility of the species in $cm^2/V\text{-}s$, ϕ_i the electrostatic potential of the species in volts, C_i is the concentration of species i in mol/cm^3, and D_i is the diffusion coefficient of the species in the electrolyte with units cm^2/s.

When, ε is defined as the porosity, u_+ and u_- are assumed to represent the mobilities of the anions and cations in $cm^2/V\text{-}sec$, ϕ_+ and ϕ_- are the given as the electrostatic potentials of the respective ions, D_+ and D_- are the actual effective diffusion coefficients of the respective ions in cm^2/s, R_+/F and R_-/F represent the number of moles per cubic cm per second of the anion and cation formed due to other processes, and $F = 96485.3\ C/mol$ is the Faraday's constant. Thus, if μ_i be the electrochemical potential of a species i expressed in J/mol, K_{ij} are friction coefficients, C_i is the concentration of species i in mol/cm^3, R is the gas constant, T is the temperature, C_T is the total sum of the concentrations of the electrolyte or solution in mol/cm^3, and v_i is the average velocity of a species I, the multi-component diffusion equation for concentrated solutions is,

$$C_i \nabla \mu_i = \sum_j K_{ij}\left(v_j - v_i\right) \qquad K_{ij} = RTC_i C_j / C_T D_{ij}$$

(3.20)

The molar flux of a species i can then be described as,

$$\mathbf{N}_i = C_i v_i$$

(3.21)

The current density of the electrolyte is given by,

$$\mathbf{i} = F(\mathbf{N}_+ - \mathbf{N}_-)$$

(3.22)

For Li-air batteries with aqueous electrolyte one has, before saturation, $R_+ = 0$, $R_- = 4R_c$ and after saturation, $R_+ = -4R_c$, $R_- = 0$. In the above R_c/F represents the rate of oxygen conversion, i.e. the molar rate of oxygen consumed per unit volume. The effective diffusion & effective conductivity constants can be defined as,

$$\kappa_D = (D_+ - D_-)FC_+, \quad \kappa_{eff} = (u_+ + u_-)FC_+$$

(3.23)

The generic charge transportation in the electrolyte for dilute solutions which is applicable to Li-air batteries with dual electrolyte before saturation is given by the equation,

$$\nabla \cdot \left[\kappa_{eff} \nabla \phi_+ + \kappa_D \nabla \ln C_+ \right] = R_- - R_+$$

(3.24)

The dilute solution theory can be applied to Li-air batteries with aqueous electrolyte, only as when the concentration of electrolyte is below saturation. The anion charge diffusion equation is,

$$\frac{\partial(\varepsilon C_+)}{\partial t} = \nabla \cdot \left(D_{eff} \nabla C_+ \right) - \frac{i \cdot \nabla t_+}{F} + \frac{t_- R_+ + t_+ R_-}{F}$$

(3.25)

where,

$$D_{eff} = \frac{u_- D_+ + u_+ D_-}{u_+ + u_-}, \quad t_+ = \frac{u_+}{u_+ + u_-}, \quad t_- = \frac{u_-}{u_+ + u_-}$$

Generic Concentrated Solution Theory

The theory of the concentrated solutions can be applied to Li-air batteries with a dual electrolyte when the concentration is beyond saturation and to Li-air batteries with an organic electrolyte (such as tetraethyl glycol di-methyl ether (TEGDME)). The Stefan-Maxwell multi-component diffusion equation, which describes the interaction of species *i* and *j*, by relating the electrochemical potential to the average velocities of species and their diffusion coefficients provides the basis for the concentrated solution theory. Thus following Bevara (Bevara, 2015), the diffusion of the anions is governed by,

$$\frac{\partial(\varepsilon C_+)}{\partial t} = \nabla \cdot \left(D_{eff} \nabla C_+\right) - \frac{i \cdot \nabla t_+}{F} + \frac{t_- R_+ + t_+ R_-}{F}$$

(3.26)

with

$$D_{eff} = D\left(1 - \frac{d\ln C_0}{d\ln C_+}\right)_, \quad t_+ = \frac{D_+}{D_+ + D_-}_, \quad t_- = \frac{D_-}{D_+ + D_-}_, \quad t_+ + t_- = 1_, \quad D = 2t_+ D_-$$

and

$$\mathbf{i} = F\left(\mathbf{N}_+ - \mathbf{N}_-\right)$$

(3.27)

Oxygen diffusion in the cathode is governed by,

$$\frac{\partial(\varepsilon C_{O_2})}{\partial t} = -\nabla \cdot \left(-D_{O_2} \nabla C_{O_2}\right) - G_{O_2}$$

(3.28)

The total ion concentration of the electrolyte is given by, $C_T = C_0 + C_+ + C_-$. For a binary electrolyte $C_+ = C_-$. The transportation of electrons or the equation for conduction is given by:

$$\nabla \cdot \left(\sigma_e \nabla \phi_e\right) + R_C = 0$$

(3.29)

Porosity of The Carbon Cathode Electrode

The cathode electrodes used in almost all Li-air batteries are made from porous carbon or graphite. Porous carbon based electrodes have several advantages including increased interfacial contact area with the electrolyte, reduced Ohmic drop in potential due to the compactness of the electrode, and the ease of contaminant filtration in the case of a flow-through electrode. The increase in the interfacial contact area counterbalances the influence of the low rate of the heterogeneous electrochemical reaction. The time dependence of porosity of the porous carbon electrode $\varepsilon(t)$, in Li-oxygen batteries with organic electrolyte is governed by,

$$\frac{d\varepsilon(t)}{dt} = -\frac{R_c}{2F} \frac{M_{Li_2O_2}}{\rho_{m, Li_2O_2}} = -\varepsilon_{0,t}$$

(3.30)

where $M_{Li_2O_2}$ and ρ_{m,Li_2O_2} are the molecular mass and mass density of Li₂O₂ and $\varepsilon_{0,t}$ is a constant. In the above R_c/F represents the oxygen conversion rate, i.e. the number of moles of oxygen consumed per unit volume and unit time. The factor 2 arises because each oxidation reaction consumes two electrons in order to form lithium peroxide. Equation (3.30) is a deterministic relation which could be analytically integrated.

The Complete Finite Difference Equations of the Distributed Model

For a standard Li-air battery with an organic electrolyte, the ion transport in the electrolyte is modelled using the concentrated solution theory. Thus the voltage output is,

$$V(t) = V_{oc} - \eta_a(t) - \eta_c(t) - (R_\Omega(t) + R_e)I \qquad (3.31)$$

where V_{oc} is the open cell voltage $\eta_c(t)$ is the over-potential at the cathode $\eta_a(t)$ is the over-potential at the anode, $R_\Omega(t)$ is the resistance of the deposit layer, R_e is the resistance of the electrolyte, and I is the value of the discharge current.

The reaction rate at the anode $r_A(t)$ is assumed to be given by Butler-Volmer equation and is used to obtain the over-potential at the anode $\eta_a(t)$. The over-potentials at the anode and the cathode are given by,

$$\eta_a = (\phi - \phi_{Li})\big|_{x=anode} - U_a \qquad (3.32)$$

$$\eta_c = (\phi - \phi_{Li})\big|_{x=cathode} - E^0 - V_{Li_2O_2} \qquad (3.33)$$

where the electrostatic potential of Li ions is ϕ_{Li} and the electrostatic potential of the electrons is ϕ.

Generally, the conductivity and diffusion related variables are given by,

$$\kappa_D = \kappa_{eff} \frac{2RT}{F}(t^+ - 1)\left(1 + \frac{df}{d\ln c_{Li}}\right) \qquad \kappa_{eff} = \varepsilon^{b_\kappa}\kappa \qquad (3.34)$$

$$D'_{Li} = D_{Li}\left(1 - \frac{d \ln c_{0,Li}}{d \ln c_{Li}}\right) \tag{3.35}$$

$$D_{O_2,eff} = \varepsilon^{b_{O_2}} D_{O_2}, \qquad D_{Li,eff} = \varepsilon^{b_{Li}} D_{Li}\left(1 - \frac{d \ln c_{0,Li}}{d \ln c_{Li}}\right) \tag{3.36}$$

where $\varepsilon^{b_{O_2}}$, ε^{b_κ}, $\varepsilon^{b_{Li}}$ are the Bruggeman constants,

The diffusion equations governing the electrostatic potential of Li ions ϕ_{Li} and the electrostatic potential of the electrons ϕ are respectively given by,

$$\nabla \cdot \left(\kappa_{eff} \nabla \phi_{Li} + \kappa_D \nabla \ln c_{Li}\right) = ar_C, \qquad \nabla \cdot \left(\sigma_{eff} \nabla \phi\right) = -ar_C \tag{3.37}$$

where a is the specific surface area of the cathode and σ_{eff} is the effective electron conductivity, κ_{eff} is the effective electrolyte conductivity and κ_D is the electrolyte's diffusion conductivity.

The concentrations of the Li and O$_2$ ions, c_{Li} and c_{O_2} respectively satisfy,

$$\frac{\partial(\varepsilon c_{Li})}{\partial t} = \nabla \cdot \left(D_{Li,eff} \nabla c_{Li}\right) - \frac{1-t^+}{F} a \times r_C - \frac{\mathbf{I}_{Li} \cdot \nabla t_+}{F} \tag{3.38}$$

$$\mathbf{I}_{Li} = -\kappa_{eff} \nabla \phi_{Li} - \kappa_D \nabla \ln c_{Li} \tag{3.39}$$

and

$$\frac{\partial(\varepsilon c_{O_2})}{\partial t} = \nabla \cdot \left(D_{O_2,eff} \nabla c_{O_2}\right) - \frac{1}{F} a \times r_C + w_k \tag{3.40}$$

where w_k is the process noise input which is assumed to be non-zero over the cathode electrode region. Only the equation (3.40) is not deterministic in the above set. Thus all of the other equations may be analytically integrated.

The time dependence of porosity of the carbon electrode in Li-oxygen batteries with organic electrolyte is governed by,

$$\varepsilon(t) = \varepsilon_0 + (t - t_0)\varepsilon_{0,t}$$

(3.41)

where ε_0 and $\varepsilon_{0,t}$ are constants. The resistance of the deposit layer is obtained in terms of the porosity by an empirical formula,

$$R_\Omega(t) = R_{\Omega 0} \exp\left(k_\Omega \left(1 - \sqrt{\varepsilon(t)/\varepsilon_0}\right)^q \right)$$

(3.42)

where $R_{\Omega 0}$, k_Ω, and q are empirical constants obtained by curve fitting as in Bevara [33]. The input could also be expressed as the specific capacity, C, per unit hour which is proportional to the discharge current I, according to the equation,

$$C = I/\left(\rho_C A L_C (1 - \varepsilon_0)\right)$$

(3.43)

where ρ_C is the mass density of the cathode material (carbon) in Kg per unit volume in cm^3, A is the cell area which is assumed to be unity and L_C is the length of the cathode. In the separator and APL regions,

$$r_C = 0 \quad \text{and} \quad \phi = 0$$

(3.44)

In the APL region the diffusion related constants are given by,

$$\kappa_{eff} = \kappa, \quad D_{Li,eff} = D'_{Li} \quad \text{and} \quad D_{O_2,eff} = D_{O_2}$$

(3.45)

The reaction rates at the anode and at the cathode are respectively given by:

$$r_A(t) = k_a \left(\exp\left(\frac{(1 - \beta')\eta_a}{V_T} \right) - \exp\left(\frac{-\beta'\eta_a}{V_T} \right) \right)$$

(3.46)

$$r_C(t) = k_c \exp\left(\frac{n(1-\beta)\eta_c}{V_T}\right)\left(\frac{c_{O_2}}{c_{O_2,ref}}\right)^{\gamma_1}\left(\frac{c_{Li}}{c_{Li,ref}}\right)^{\gamma_2}$$

(3.47)

where $V_T = RT/F$ is the thermal voltage, k_a, k_c, γ_1, γ_2 are the reaction rate related constants and, β and β' are symmetry factors. $c_{Li,ref}$ and $c_{O_2,ref}$ are reference values of the ionic concentrations of the Li and oxygen ions.

The boundary conditions at $x = L$ (the air side) are, $\mathbf{I}_{Li} = 0$, $\mathbf{N}_{Li} = 0$, $c_{O_2} = sc_{O_2}^{ext}$, s is the solubility factor, $\mathbf{I}_e = I$. Hence $c_{O_2} = sc_{O_2}^{ext}$, $\nabla c_{Li} = 0$, $\nabla \phi_{Li} = 0$, $\nabla \phi = -I/\sigma_{eff}$. The boundary conditions at the interface $x = L_{sep}$ are, $\mathbf{I}_e = 0$, Hence $\nabla \phi = 0$. The boundary conditions at the Li metal side, $x = 0$, are, $\mathbf{I}_{Li} = -r_A$, $c_{Li} = c_{0,Li}$, $\mathbf{N}_{O_2} = 0$. Hence, $c_{Li} = c_{0,Li}$, $\nabla c_{O_2} = 0$ and $\nabla \phi_{Li} = $ specified .

The one-dimensional Poisson equation is solved following the central difference approximation of the gradient, using the well-known Thomas algorithm. The unsteady one-dimensional diffusion equations are reduced to the Poisson equation by approximating the time derivative by an explicit, backward difference approximation. The state vector of the entire model is made up of the anion concentrations at the finite difference grid points, the oxygen ion concentrations at the same grid points and the porosity of the carbon electrode. The input is the discharge/charge current I, which is positive during discharge, and is assumed to be known precisely.

Reduced Order Modelling of a Li-Air Cell

To construct a reduced order model it is first recognized that anodic over-potential influences the ionic concentrations only through the boundary condition at the anode. Thus it is possible in principle to approximate the anodic overpotential distribution across the cell. Further ionic concentrations of the Li-ions are only weakly coupled to the concentrations of the oxygen ions and to the cell output voltage. Moreover, they and the concentrations of the oxygen ions outside the cathode electrode may be treated as deterministic processes. Thus only the ionic concentrations of the oxygen ions within the cathode are modelled as uncertain or non-deterministic processes. In most cell designs only the region of the cathode in the vicinity of the gas inlet is relevant, for facilitating oxygen ion transport into the electrolyte. For this reason, the basic assumption that it is the concentration of oxygen ions that plays a key role in determining the output is a reasonable one.

Reduced oxygen ion transport in the cathode electrode can be further accentuated by pore-clogging, i.e., the obstruction of the pathways to oxygen ion-diffusion. Oxygen transport limitations can lead to an instantaneous drop in the cell voltage output. Yet it must be said that

there are fundamental limits to the transport rates governed by the solubility and diffusivity (i.e., permeability) of oxygen ions in the electrolyte. The dynamics of oxygen ion transport is governed by the time dependent diffusion equation (3.40). The uncertainty in the oxygen ion concentrations is assumed to be uniform and modelled by constant intensity, independent, White noise processes across the cathode. The measurement, the cell output voltage is also assumed to be corrupted by a constant intensity White noise process. Following Bevara (Bevara, 2015), the cell output voltage is expressed as,

$$V(t) = V_{oc} - (R_{\Omega}(t) + R_e)I + v_k$$

$$- \frac{V_t}{\beta}\left(\sinh^{-1}\left(\frac{I}{2Ak_a} \right) + \sinh^{-1}\left(\frac{I \times r_{p,0}}{4AL_Ck_c}\left(\frac{c_{O_2,ref}}{\bar{c}_{O_2}} \right)\sqrt{\frac{1}{\varepsilon_0\varepsilon(t)}} \right) \right)$$

(3.48)

where $r_{p,0}$ is the mean pore radius, v_k is the measurement noise and $\bar{c}_{O_2}$ is the mean of the concentration of the oxygen ions c_{O_2}, across the cathode.

Table 3.1. Parameters used to simulate the Li-Air cell

dx	0.1 mm	Δt	0.1 milli sec
F	96485.3	R	8.3143
T (cell temperature)	$300°K$	ρ_C (carbon density)	$2.26\,g/cm^3$
t_{APL} (APL thickness)	$1 \times dx$	ρ_e (electron density)	$1.2\,g/cm^3$
t_{sep} (separator thickness)	$50 \times dx$	t_{cat} (cathode thickness)	$200 \times dx$
$c_{O_2,ref}$	$0.001/cm^3$	$c_{Li,ref}$	$0.001/cm^3$
$c_{O_2,ext}$	$9.42 \times 10^6/cm^3$	c_{Li0}	$0.001/cm^3$
$\varepsilon^{bO_2} = \varepsilon^{b\kappa} = \varepsilon^{bLi}$	1.5	ε_0	0.75
γ_1	1	γ_2	2
$\beta = \beta'$	0.5	V_{oc}	2.98
$M_{Li_2O_2}$	$45.88g/mol$	ρ_{m,Li_2O_2}	$2.31g/cm^3$
k_a	1.26×10^{-3}	k_c	1.7×10^{-8}
R_e	0.001	s	0.345
σ_{eff}	1	D_{O_2}	$4 \times 10^{-5}\,cm^2/s$
a	1	$R_{\Omega 0}$	1000

| k_Ω | 4 | q | 1 |
| $r_{p,0}$ | $20 \times 10^{-7} \, cm$ | κ | $11.41 \times 10^{-3} \, S/cm$ |

Typical Simulation Based Response of a Li-Air Cell

The example considered is a single Li-air cell operating at the room temperature of 22°C. The stochastic dynamic model developed for several applications is given by equations for the oxygen ion concentration in the cathode which could be obtained from (3.42). The measurement variable defined by equation (3.48). The complete set of parameters used to represent the model equations are listed in Table I. Both the, structural (porosity, mean pore radius, specific surface area, tortuosity) and the physical properties (permeability, electrical resistance) of the electrodes obtained by a variety of porosimetry and permeability based techniques were used obtain the electrical properties of the cathode.

In Figure 3.5 the simulated voltage characteristics of a Li-air cell over a half a second time for discharge currents ranging from 1 to 625 milliamps are shown. In this simulation the process noise inputs were assumed to be zero. The increase in the discharge current results in a marked reduction in the output cell voltage due to the decrease in the effective porosity. The effect of starving the cell of oxygen by reducing the oxygen available to 10% of that in Figure 3.3, is shown in Figure 3.4.

Fig. 3.3.   Simulated voltage characteristics of a Li-air cell over a half a second time frame with discharge currents ranging from 1 to 625 milliamps.
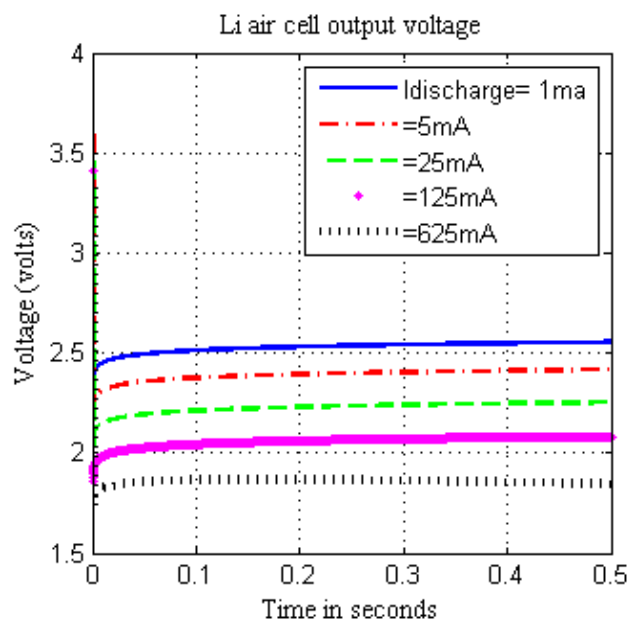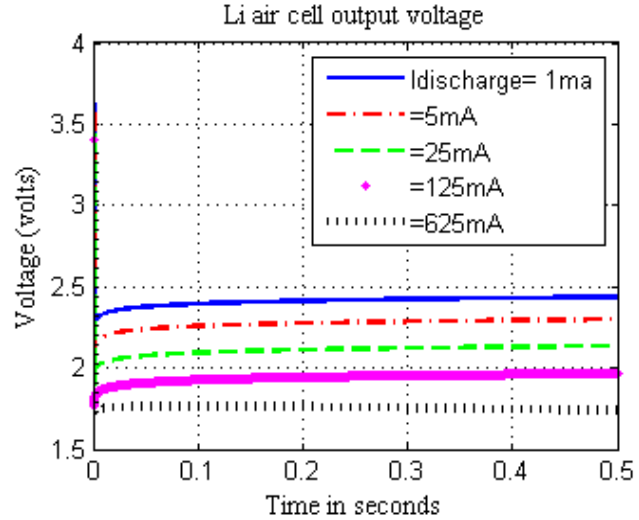
Fig. 3.4. Simulated voltage characteristics of a Li-air cell with reduced oxygen and with a discharge current ranging from 1 to 625 milliamps

Li air cell output voltage

The energy and power density of a battery can generally be improved by minimising undesirable microstructure induced polarisation losses associated with interfacial, concentration and Ohmic effects. Tortuous transport paths, i.e. paths with twists and turns, result in a higher overall Ohmic resistance, which in turn restricts the delivered energy and power density. In our work we have used nominal values for the specific surface area and the porosity, for the porous carbon electrode, as the values used for three-dimensional electrodes, in the literature vary substantially. Yet it can be confirmed on the basis of the results illustrated in the preceding section that the methodology of using a discrete time model for the concentration of the oxygen ions provides a valid model for obtaining not only the output of the cell but also the actual concentration of the oxygen ions in the cathode region. It has not only been possible to predict the cell output but also been able to show the reduction in the cell output due to the decrease in the effective porosity of the carbon electrode.

The pressure drop across the electrode is modelled by the Ergun equation, as a function of the fluid velocity or the interstitial Reynolds number and describes the dissipation of mechanical energy in the flow through a porous medium. By considering the tortuosity which is a measure of the fluid path length through the porous material related to the actual path length through the carbon material, and the pressure drop across the electrode, it is possible in principle to monitor the porosity of the carbon electrode. However, such methods require accurate a priori estimates of concentrations of the oxygen and also of the Li ions. Thus, we expect our method of simulation of the cell output and the ionic concentrations to aid the process of monitoring the electrode porosity which in turn will make it feasible to predict or estimate the state of charge of a Li-air cell. In conclusion, our model is capable of providing not only reliable solutions to battery output as a function of the battery's internal states, the material parameters and the battery's geometric and physical parameters but also the concentration distribution of the oxygen ions within the electrolyte.

Fault Detection in Batteries

Electric vehicle battery types are Lead-acid, Nickel metal hydride, Zebra, and Lithium-ion. Lithium-ion batteries are among the growing electric power sources and must be maintained within acceptable operating conditions to ensure high efficiency and reliability. Hence, a robust fault detection and isolation scheme is required to determine when sensor or actuator faults take place as a threat to the health of the battery. For instance, a current sensor fault leads to erroneous estimates of state of charge and other parameters, which in turn affects the control actions in the battery management system (BMS). A temperature sensor fault may lead to ineffective thermal management.

A Li-ion battery pack in an electric vehicle (EV) consists of hundreds of cells and requires a battery management system (BMS). The BMS plays an important role in ensuring a safe and reliable operation of the battery in EVs. Generally, battery performance testing includes the determination of: State of Charge (SOC), State of Health (SOH), and Energy Efficiency.

Fault detection is an important task in the BMS and is responsible for detecting faults as early as possible and providing control actions to minimise fault effects, to ensure the safe and reliable operation of the battery system. The residual signals need to be generated to detect deviations from the standard behaviour. An equivalent circuit methodology is used to construct the battery models. There are several model-based techniques in the literature to generate the residuals such as multiple model adaptive estimation technique (Kalman Filtering based), sliding mode observers etc.

The state of charge of Li-Ion batteries may be estimated via Kalman filters and the residuals are generated to detect any abnormality in the standard behaviour. Since electric vehicles are becoming popular, the research has also increased on batteries and fault issues of batteries. Some research examples are summarised as follows.

Marcicki et al. (Marcicki et al, 2010) have formulated a diagnostic problem as a nonlinear parity equation approach. Sliding mode observers are designed for input estimation, while the output voltage estimation is performed using an open loop model. The selection of optimal thresholds given a maximum allowable probability of error is also considered. The estimation error of the observers determines a lower bound on the minimum detectable fault magnitude.

Singh et al. (Singht et al, 2013) have developed a battery fault detection unit using multiple model adaptive estimation techniques. Impedance spectroscopy data from Li-ion cells is used along with the equivalent circuit methodology to construct the battery models. Battery faults such as overcharge and over discharge cause significant model parameter variation and can be considered as separate models. Kalman filters are used to estimate the parameters of each model and to generate the residual signal. These residuals are then used in the multiple model adaptive estimation technique to detect battery faults. Simulation results show that by using this method the battery faults can be detected in real-time, thus providing an effective way of diagnosing Li-Ion battery failure.

Dey et al. (Dey et al, 2016) have presented a model-based diagnostic scheme that uses sliding mode observers designed based on the electrical and thermal dynamics of the battery. It is analytically shown how the extraction of the equivalent output error injection signals on the sliding manifolds enables the detection, the isolation, as well as the estimation of the temperature, voltage, and current sensor faults. This brief includes simulation and experimental studies to demonstrate and evaluate the effectiveness of the proposed scheme.

Ablay (Ablay et al, 2013) has designed an observer-based fault diagnosis approach to analyse the state of health of the Ni-MH battery system of hybrid electric vehicles (HEVs). Real-world input data is used to assess the efficiency of the approach in the existence of uncertainties. The possible sensor faults and unexpected parameter deviations are diagnosed efficiently with statistical evaluation of the generated residuals.

Wu et al. (Wu et al, 2015) have reviewed recent research and development of ageing mechanisms of Li-ion batteries to understand the origins and symptoms of Li-ion battery faults. Through ageing tests, relationship between performance and ageing factors, as well as cross-dependence among factors can be quantified. The advantages and disadvantages of the fault diagnosis technology for Li-ion batteries are summarised.

Kong et al. (Kong et al, 2018) investigate estimation and fault diagnosis of fractional-order Lithium-ion battery systems. Two simple and common types of observers are designed to address the design of fault diagnosis and estimation for the fractional-order systems. The paper presents some theoretical results for designing stable observers and fault estimators. Overall, the design of the Luenberger observer as well as the sliding mode observer can be used in fault detection, fault isolation, and estimation.

Kang et al. (Kang et al, 2000) have proposed an online multi-fault diagnostic method based on a non-redundant crossed-style measurement circuit and improved correlation coefficient method. The correlation coefficient method is used to catch fault signatures and assess the fault degree. By applying these two methods, the cell faults can be distinguished from other faults by identifying the correlation coefficient of neighbouring voltages with fault flags. Furthermore, connection faults and voltage sensor faults are isolated by the correlation coefficient of the neighbouring voltages difference and current.

Alavi et al. (Alavi et al, 2019) focus on the residual-based fault detection and isolation (FDI) in batteries, power electronics and chargers. Currently, isolation of multiple faults is performed by generating a bank of residuals, one residual signal for each fault. It is shown that, with a combination of different residual evaluation functions, various battery and electronics faults, including battery short/open circuit, sensor biases, input voltage drop, and switches short/open circuit, can be detected and isolated by using the magnitude and slope of a residual signal or its norm generated by the battery voltage.

Mina et al. (Mina et al, 2018) present a connecting fault detection method of lithium-ion power batteries in series. The cross-voltage test is adopted to distinguish contact resistance increases and internal resistance increases fault. The experimental battery based on first-order

resistance and capacitance (RC) equivalent circuit and MATLAB/Simulink platform is simulated. The mean square error which indicates the difference between experiment and simulation is employed to describe the voltage state of the cell. If the abnormal voltage exists, it is concluded that a fault occurs through analysing the voltage abnormal coefficients based on modified Z-score, which is considered as a second-degree fault. The temperature rise rate is regarded as a secondary parameter to determine whether the second-degree fault deteriorates into a first-degree fault. According to different levels of failure, the battery management system reminds users to take appropriate measures in practice.

Hu et al. (Hu et al, 2020) provide a comprehensive review of fault mechanisms, fault features, and fault diagnosis of various faults in Lithium-Ion Battery Systems (LIBS), including internal battery faults, sensor faults, and actuator faults. Future trends in the development of fault diagnosis technologies for a safer battery system are presented and discussed.

Tran in his thesis (Tran et al, 2020) shows that degradation can affect the long-term performance of the battery and its model parameters, hence it can cause false fault detection in state observer FDI schemes. This thesis also presents a novel model-based sensor FDI scheme for a Li-ion cell that takes into consideration battery degradation. The proposed scheme uses the recursive least squares (RLS) method to estimate the equivalent circuit model (ECM) parameters in real-time. The estimated ECM parameters are put through weighted moving average (WMA) filters, and then cumulative sum control charts (CUSUM) are implemented to detect any significant deviation between unfiltered and filtered data, which would indicate a fault. The current and voltage sensor faults are isolated based on the responsiveness of the parameters when each fault occurs.
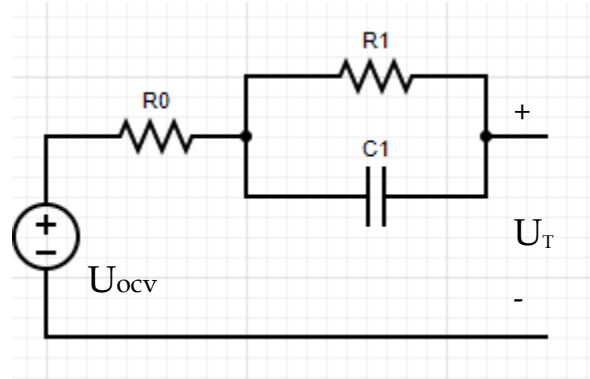
A circuit model of a Li-Air battery is presented below,

Fig. 3.5   Model of Li-Air battery
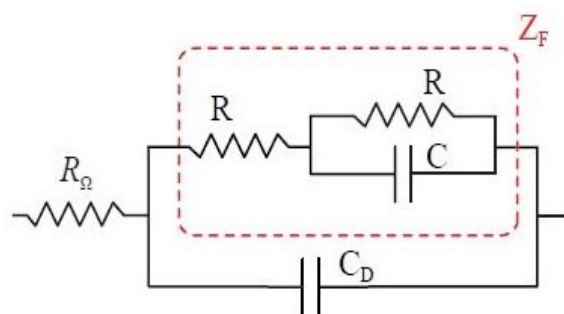
If C_D is neglected the equivalent circuit turns out to be,

Fig. 3.6.   Equivalent Circuit

where $R_0 = (R_\Omega + R)$, $R_1 = R$, $C_1 = C$.

Then, the Kirchhoff equations for the circuit above are;

$$UT = UOCV - U_1 - R_0 I_L \qquad (3.49)$$

$$C\frac{dU_1}{dt} = -\frac{U_1}{R} + I_L \qquad (3.50)$$

The simulation results in the figure below shows that the estimation of state of charge by Kalman filter converges to the real state of charge. Following true estimations, the residuals can be generated based on the estimation error. In the above scenario there is no fault and obviously the residual is very small (Sen, 2019).
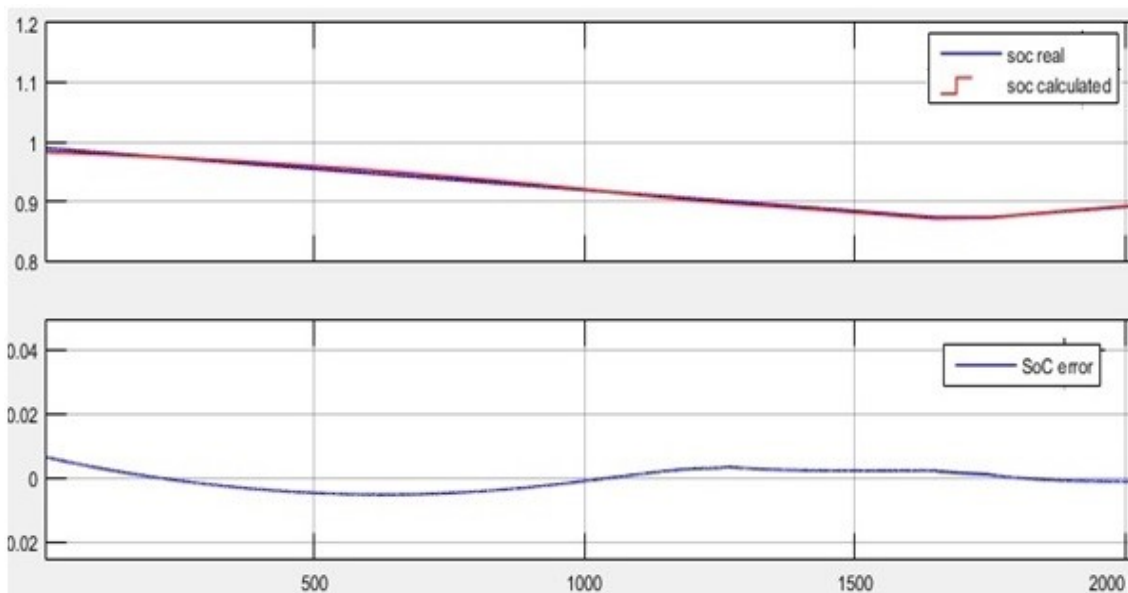

Fig. 3.7.   Upper graph: Real battery state of charge, and Kalman filter estimation of battery state of charge. Lower graph: The estimation error between real and estimated values.

3.4 Conclusion

In this paper, one of clean propulsion system technologies for future air transport is emphasised. This review paper describes the state-of-the-art on hybrid propulsion component modelling for two key components: a high-temperature superconducting permanent magnet synchronous motor and a lithium-air battery that could be essential in delivering a clean and efficient energy source for propelling an electric aircraft in the future. It can be seen from the literature studies that specific energy of batteries and specific power of electronics will have a deep impact on all future's electric propulsion designs. Development and servicing process of novel propulsion systems will heavily depend on the technological developments in this area. Furthermore, simulation and demonstrations dependent on mathematical models will be important parts of manufacturing processes in terms of developing effective, efficient, and clean future vehicle propulsion systems. Mathematical models and simulations will also make contribution to the sector by means of providing unmeasurable data, saving time, being economical, testing flightworthy, optimising and updating designs before manufacturing and so on. In the upcoming studies, it is planning to simulate mathematical models of all novel architectures as a whole combining new technologies of each component.

Conflicts of Interest: The authors declare there are no conflicts of interest.

References

Ablay G (2013). "An observer-based fault diagnosis in battery systems of hybrid vehicles". 2013 8th International Conference on Electrical and Electronics Engineering (ELECO), Bursa, Turkey, pp.238-242.

Alavi SMM, Fekriasl S, Niyakan SN et al (2019) "Fault detection and isolation in batteries power electronics and chargers". Journal of Energy Storage, 25 (2019):1-9.

Armstrong M. J., Blackwelder M., Bollman A. et al (2015) "Architecture, Voltage, and Components for a Turboelectric Distributed Propulsion Electric Grid Final Report". NASA/CR—2015-218440.

Baumeister S., Leung A and Ryley T(2020) The emission reduction potentials of First Generation Electric Aircraft (FGEA) in Finland, Journal of Transport Geography, 85: 102730, ISSN 0966-6923, https://doi.org/10.1016/j.jtrangeo.2020.102730.

Bevara VV (2015) Modeling and Simulation of Metal-Air Batteries, PhD Dissertation, The Graduate School, Department of Electrical and Computer Engineering, FAMU-FSU College of Engineering, Florida State University.

Brelje BJ and Martins JRRA (2019) Electric, hybrid, and turboelectric fixed-wing aircraft: A review of concepts, models, and design approaches, Progress in Aerospace Sciences, 104: 1-19, ISSN 0376-0421, https://doi.org/10.1016/j.paerosci.2018.06.004.

72

Chen G, MaA D, Jia Y, et al (2021) Comprehensive sizing and optimization method for series-hybrid unmanned convertiplane, Chinese Journal of Aeronautics, 34(4): 387-402 ISSN 1000-9361, https://doi.org/10.1016/j.cja.2020.07.016.

Dey S, Mohon S, Pisu P, Ayalew B (2016). "Sensor Fault Detection, Isolation, and Estimation in Lithium-Ion Batteries". IEEE Transactions on Control Systems Technology, Volume: 24, Issue: 6, Nov. 2016, pp. 2141-2149.

Donateo T, Ficarella A., Spedicato L. (2016) Development and validation of a software tool for complex aircraft powertrains. Advances in Engineering Software, 96: 1-13, ISSN 0965-9978, https://doi.org/10.1016/j.advengsoft.2016.01.001.

Donateo T, Spedicato L, Placentino DP (2017) Design and performance evaluation of a hybrid electric power system for multicopters, Energy Procedia,126: 1035-1042, ISSN 1876-6102, https://doi.org/10.1016/j.egypro.2017.08.310.

Donateo T and Spedicato L (2017) Fuel economy of hybrid electric flight, Applied Energy, 206: 723-738, ISSN 0306-2619, https://doi.org/10.1016/j.apenergy.2017.08.229.

Donateo T, Carlà A and Avanzini G (2018) Fuel consumption of rotorcrafts and potentiality for hybrid electric power systems, Energy Conversion and Management, 164:429-442, ISSN 0196-8904, https://doi.org/10.1016/j.enconman.2018.03.016.

Gemin, P., Kupiszewski, T., Radun, A. et al (2015). Architecture, Voltage, and Components for a Turboelectric Distributed Propulsion Electric Grid (AVC-TeDP). NASA/CR-2015-218713

Gnadt AR, Speth RL, Sabnis JS et al (2019) Technical and environmental assessment of all-electric 180-passenger commercial aircraft, Progress in Aerospace Sciences, 105:1-30, ISSN 0376-0421, https://doi.org/10.1016/j.paerosci.2018.11.002.

Gong A, Palmer JL, Brian G, et al (2016) Performance of a hybrid, fuel-cell-based power system during simulated small unmanned aircraft missions, International Journal of Hydrogen Energy, 41(26): 11418-11426, ISSN 0360-3199, https://doi.org/10.1016/j.ijhydene.2016.04.044.

Hu X, Zhang K, Liu K, et al (2020). "Advanced Fault Diagnosis for Lithium-Ion Battery Systems: A review of Fault Mechanisms, Fault Features and, Dİagnosis Prosedures IEEE Industrial Electronics Magazine, 14(3):65-91

Ji Z, Qin J, Cheng K, et al (2020) Performance characteristics of a solid oxide fuel cell hybrid jet engine under different operating modes, Aerospace Science and Technology, 105 :106027, ISSN 1270-9638, https://doi.org/10.1016/j.ast.2020.106027.

Ji Z, Qin J, Cheng K et al (2020) Determination of the safe operation zone for a turbine-less and solid oxide fuel cell hybrid electric jet engine on unmanned aerial vehicles, Energy, 202(6) :117532, ISSN 0360-5442, https://doi.org/10.1016/j.energy.2020.117532.

Kang Y, Duan B and Zhou Z Yunlong Shang, Chenghui Zhang et al (2000). "Online multi-fault detection and diagnosis for battery packs in electric vehicles". Applied Energy, 259:1-16, 114170.

Kong S, Saif M, and Cui G (2018). "Estimation and Fault Diagnosis of Lithium-Ion Batteries: A Fractional-Order System Approach". Hindawi Mathematical Problems in Engineering, 2018: 8705363, 12 pages.

Marcicki J, Onori S and Rizzoni G (2010). "Nonlinear fault detection and isolation for a lithium-ion battery management system ". Proceedings of the ASME 2010 Dynamic Systems and Control Conference DSCC2010 September 12-15, 2010, Cambridge, Massachusetts, USA pp. 607-614.

Mina M, Yu W, Qiangling D et al (2018) "Fault detection of the connection of lithium-ion power batteries in series for electric vehicles based on statistical analysis". Energy, 164: 745-756.

National Academies of Sciences, Engineering, and Medicine. 2016. Commercial Aircraft Propulsion and Energy Systems Research: Reducing Global Carbon Emissions. Washington, DC: The National Academies Press. https://doi.org/10.17226/23490.

Ozcira S and Bekiroglu N (2011) Direct Torque Control of Permanent Magnet Synchronous Motors, Chapter 6, in Torque Control, Prof. Moulay Tahar Lamchich (Ed.), InTech, ISBN: 978-953-307-428-3.

Pornet C and Isikveren A.T. (2015) Conceptual design of hybrid-electric transport aircraft, Progress in Aerospace Sciences, 79: 114-135, ISSN 0376-0421, https://doi.org/10.1016/j.paerosci.2015.09.002.

Ribeiro J, Afonso F, Ribeiro I et al (2020) Environmental assessment of hybrid-electric propulsion in conceptual aircraft design, Journal of Cleaner Production, 247:119477, ISSN 0959-6526, https://doi.org/10.1016/j.jclepro.2019.119477.

Riboldi CED, Gualdoni F, Trainelli L (2018) Preliminary weight sizing of light pure-electric and hybrid-electric aircraft, Transportation Research Procedia, 29: 376-389, ISSN 2352-1465, https://doi.org/10.1016/j.trpro.2018.02.034.

Riboldi CED (2018) An optimal approach to the preliminary design of small hybrid-electric aircraft, Aerospace Science and Technology, 81: 14-31, ISSN 1270-9638, https://doi.org/10.1016/j.ast.2018.07.042.

Riboldi CED (2019) Energy-optimal off-design power management for hybrid-electric aircraft, Aerospace Science and Technology, 95: 105507, ISSN 1270-9638, https://doi.org/10.1016/j.ast.2019.105507.

Roboam X (2011) New trends and challenges of electrical networks embedded in "more electrical aircraft", 2011 IEEE International Symposium on Industrial Electronics, Gdansk, pp. 26-31, doi: 10.1109/ISIE.2011.5984130.

Rohacs J and Rohacs D (2020) Energy coefficients for comparison of aircraft supported by different propulsion systems, Energy, 191:116391, ISSN 0360-5442, https://doi.org/10.1016/j.energy.2019.116391.

Xie Y, Savvaris A and Tsourdos A (2019) Fuzzy logic based equivalent consumption optimization of a hybrid electric propulsion system for unmanned aerial vehicles, Aerospace Science and Technology, 85:13-23, ISSN 1270-9638, https://doi.org/10.1016/j.ast.2018.12.001.

Xie Y, Savvarisal A, Tsourdos A et al (2021), Chinese Journal of Aeronautics, 34(4):432-450 ISSN 1000-9361, https://doi.org/10.1016/j.cja.2020.07.017.

Sen, B. (2019) "Modeling and State of Charge Estimation of Metal-Air Batteries by Kalman Filter for the Usage in Electric Vehicles", MSc Thesis, Istanbul Technical University.

Sener, E., Yazar, I. and Ertasgin, G (2020) "Single Turboshaft Engine Failure Analysis of an Inner Bus Ties Architecture for Turboelectric Distributed Propulsion System", SAE International Journal of Aerospace, 13(2):155-170

Sener, E, Yazar, I, Ertasgin, G. et al (2020) "Baseline Architecture Design for a Turboelectric Distributed Propulsion System Using Single Turboshaft Engine Operational Scenario", International Journal of Turbo & Jet Engines (In press).

Singh A, Izadian A and Anwar S (2013). "Fault diagnosis of Li-Ion batteries using multiple-model adaptive estimation". IECON 2013 - 39th Annual Conference of the IEEE Industrial Electronics Society Vienna, Austria, pp. 3524-3529.

Sliwinski J, Gardi A, Marino M et al (2017) Hybrid-electric propulsion integration in unmanned aircraft, Energy, 140(Part2):1407-1416, ISSN 0360-5442, https://doi.org/10.1016/j.energy.2017.05.183.

Sziroczak D, Jankovics I, Gal I, et al (2020) Conceptual design of small aircraft with hybrid-electric propulsion systems, Energy, 204: 117937, ISSN 0360-5442, https://doi.org/10.1016/j.energy.2020.117937.

Tay G, Keller P, Hornung M (2018) Development of a software tool for comprehensive flight performance and mission analysis of hybrid-electric aircraft. Transportation Research Procedia, 29: 401-409, ISSN 2352-1465, https://doi.org/10.1016/j.trpro.2018.02.036.

Tran M (2020). Sensor Fault Detection and Isolation for degrading LİB in electric vehicles". Msc Thesis, Waterloo University.

Vepa R (2018) Modeling and Dynamics of HTS Motors for Aircraft Electric Propulsion, Aerospace (MDPI), 5(1):21 http://www.mdpi.com/2226-4310/5/1/21/pdf

Vratny PC and Hornung M (2018) Sizing Considerations of an Electric Ducted Fan for Hybrid Energy Aircraft, Transportation Research Procedia, 29: 410-426, ISSN 2352-1465, https://doi.org/10.1016/j.trpro.2018.02.037.

Wu C, Zhu C and Ge Y et al (2015) "A Review on Fault Mechanism and Diagnosis Approach for Li-Ion Batteries" Hindawi Publishing Corporation Journal of Nanomaterials Volume 2015: 631263, 9 pages.

Yazar, I. (2019), "Simulation of a High Fidelity Turboshaft Engine-Alternator Model for Turboelectric Propulsion System Design and Applications", International Journal of Turbo & Jet-Engines, 36(3):271–281, eISSN 2191-0332, ISSN 0334-0082, DOI: https://doi.org/10.1515/tjj-2018-0036.